Check for updates

Geophysical Research Letters

RESEARCH LETTER
10.1029/2022GL100166

Key Points:

- Real Time Kinematics measurements of civilian networks capture near-field coseismic displacements of the 2020 strike-slip Petrinja earthquake
- Time-series from regional continuous GNSS stations constrain coseismic deformation in the far-field
- Elastic modeling argues for two slip patches on the main fault and for significant slip on a parallel secondary fault

Supporting Information:

Supporting Information may be found in the online version of this article.

Correspondence to:

M. Henriquet and B. Kordic,
henriquet@cerege.fr;
bkordic@hgi-cgs.hr

Citation:

Henriquet, M., Kordic, B., Métois, M., Lasserre, C., Baize, S., Benedetti, L., et al. (2022). Rapid remeasure of dense civilian networks as a game-changer tool for surface deformation monitoring: The case study of the M_w 6.4 2020 Petrinja earthquake, Croatia. *Geophysical Research Letters*, *49*, e2022GL100166. https://doi.org/10.1029/2022GL100166

Received 28 JUN 2022
Accepted 23 NOV 2022

Author Contributions:

Conceptualization: M. Métois, C. Lasserre
Data curation: B. Kordic, M. Spelić, M. Vukovski
Formal analysis: M. Henriquet, M. Métois
Funding acquisition: M. Métois
Investigation: B. Kordic
Methodology: M. Henriquet, B. Kordic, M. Métois, C. Lasserre
Project Administration: S. Baize
Software: M. Henriquet, M. Métois

© 2022 The Authors.
This is an open access article under the terms of the Creative Commons Attribution-NonCommercial License, which permits use, distribution and reproduction in any medium, provided the original work is properly cited and is not used for commercial purposes.

Rapid Remeasure of Dense Civilian Networks as a Game-Changer Tool for Surface Deformation Monitoring: The Case Study of the M_w 6.4 2020 Petrinja Earthquake, Croatia

M. Henriquet[1], B. Kordic[2], M. Métois[3], C. Lasserre[3], S. Baize[4], L. Benedetti[1], M. Spelić[2], and M. Vukovski[2]

[1]Aix Marseille Université, CNRS, IRD, Collège de France, CEREGE, Aix-en-Provence, France, [2]Croatian Geological Survey (HGI-CGS), Zagreb, Croatia, [3]Université de Lyon, UCBL, ENSL, UJM, CNRS, LGL-TPE, Villeurbanne, France, [4]Institut de Radioprotection et de Sûreté Nucléaire, IRSN, PSE-ENV, SCAN/BERSSIN, Fontenay-Aux-Roses, France

Abstract The M_w 6.4 right-lateral Petrinja earthquake (2020, Croatia) is one of the largest continental earthquakes of central Europe for decades. The slip pattern of such events is usually difficult to retrieve with terrestrial geodesy due to limited monitoring means. This study takes advantage of a unique data set of dense measurements of coseismic displacement in the epicentral area, obtained by repeated measurements of benchmark networks designed for civilian purposes, and supplemented by far-field continuous GNSS measurements. Elastic modeling of these data shows two coseismic slip patches that extend over a 15 × 10 km rupture plane, locally reaching the surface, and that a right-lateral sub-parallel secondary fault in the central part of the rupture likely accommodated part of the coseismic deformation. This study demonstrates that rapid re-measurement of pre-existing civilian networks offers unique coseismic constrains in the near-field where InSAR or optical image correlation may decorrelate.

Plain Language Summary The magnitude 6.4 Petrinja earthquake that stroke Croatia on 29 December 2020, is one of the largest earthquakes registered for decades in continental Europe. Large damage and surface ruptures were observed, suggesting that the earthquake occurred at a very shallow depth. The slip pattern for such moderate magnitude earthquakes is usually difficult to retrieve with terrestrial geodesy because of limited monitoring means and small deformations. In this study, we use a unique data set made of dense coseismic displacement estimates in the epicentral area obtained by repeated positioning measurements of benchmark networks designed for civilian purposes. The inversion of this displacement field completed by far-field continuous GNSS measurements shows that the coseismic slip on the Petrinja-Pokupsko fault is limited to depths no greater than 10 km and has reached the surface locally. A single-fault model explains well the data, but the fit is largely improved with a sub-parallel secondary fault in the central part of the rupture. This study demonstrates that quick remeasurement of pre-existing civilian networks can offer unique constrains on the coseismic deformation and the associated fault geometry when spatial techniques such as InSAR or optical correlation may decorrelate.

1. Introduction

The M_w 6.4 Petrinja earthquake is the mainshock of a seismic sequence that ruptured the Petrinja-Pokupsko Fault (PPKF) in northwestern Croatia on December 2020. This is the strongest event ever recorded in this region since the $M \approx 6.3$ Zagreb earthquake in 1880 (see Figure 1 and Markušić et al. (2020)). It is also one of the largest intra-continental earthquakes in Europe since the M_w 6.5 Norcia earthquake, 2016 (Central Italy, Chiaraluce et al. (2017)), and the M_w 6.4 Dürres earthquake, 2019 (Albania, Ganas et al. (2020)), all surrounding the Adriatic microplate.

Northern Croatia is a transitional domain between the Alps, the Dinarides, and the Pannonian basin (Figure 1). The kinematics of this peri-Adriatic domain is characteristic of a low strain region with <5 mm/yr of NE-SW compression distributed over more than 150 km (Figure 1, Metois et al. (2015)). This contraction is mostly accommodated along the External Dinarides belt, but also in the Dinarides-Pannonian transition zone (Nocquet, 2012). The seismicity of NW Croatia is mainly localized along the NW-trending transpressive PPKF and the NE-trending Medvenica thrust system (Herak et al., 2009; Prelogović et al., 1998; Tomljenović & Csontos, 2001). Several

19448007, 2022, 24, Downloaded from https://agupubs.onlinelibrary.wiley.com/doi/10.1029/2022GL100166 by Cochrane France, Wiley Online Library on [17/12/2022]. See the Terms and Conditions (https://onlinelibrary.wiley.com/terms-and-conditions) on Wiley Online Library for rules of use; OA articles are governed by the applicable Creative Commons License

Supervision: M. Métois, L. Benedetti
Validation: C. Lasserre
Writing – original draft: M. Henriquet, M. Métois
Writing – review & editing: B. Kordic, C. Lasserre, S. Baize, L. Benedetti

historical destructive earthquakes occurred on these faults (Figure 1), including the famous 1909 M5.8 Kupa Valley earthquake that ruptured the PPKF system ∼20 km NW of Petrinja (Herak & Herak, 2010).

The 2020 Petrinja seismic sequence started on 28 December with a M_L 5.0 foreshock which occurred 29 hr 51 min before the main shock on the PPKF and 2 km SW of it (Baize et al., 2022). Focal mechanisms and the aftershock sequence (Baize et al., 2022) as well as the early InSAR-based slip inversion models (Ganas et al., 2021; Xiong et al., 2022) are all consistent with a steeply SW-dipping source (>70°) at shallow depth (3–13 km), which could explain the severe damage reported (Markušić et al., 2021). However, preliminary InSAR-based models could not fully capture the along-strike variations of the slip pattern due to InSAR decorrelation in the near-field (see Figure S1 in Supporting Information S1) and the use of uniform slip models (Ganas et al., 2021).

Shortly after the 2020 Petrinja earthquake, a collaborative European team mobilized to inventory coseismic ground effects in the epicentral area (Baize et al., 2022), such as landslides, liquefaction and surface ruptures. A NW-trending and segmented surface rupture was observed over ∼13 km, with an average dextral slip of ∼10 cm, locally reaching up to 38 cm (Baize et al., 2022). Field mapping highlighted a multi-kilometer en échelon right-stepping geometry along the NW-striking PPKF (Figure 2). During the weeks and months following the earthquake, this collaborative work led to rapid-static measurements of dense networks of benchmarks in the very near-field of the fault (raw data set presented in Kordić et al. (2021) and Baize et al. (2022)). These benchmarks were initially built for civil engineering, cadastral, topographic, and leveling applications. Although these measurements are of lower quality than those at continuous or survey GNSS sites (centimeter accuracy (Hastaoglu & Sanli, 2011; Pesci et al., 2008)), their high spatial density offers a unique opportunity to map surface deformation in the epicentral area.

In the present study, we take advantage of this unique geodetic data set, supplemented with measurements of far-field coseismic displacements (named "coseismic offsets" hereafter) from high-precision continuous GNSS time-series, to refine the coseismic slip model of the earthquake. In the following, we describe the data sets used and their processing, present the main outcomes of the elastic inversions of the coseismic surface displacement field, and finally discuss the slip distribution pattern with regard to the local characteristics of the PPKF.

2. Data Acquisition and Processing

We use data of 15 GNSS stations operating continuously in the region and a set of 169 pre-post earthquake benchmarks' positions (Figures 1 and 2). We describe below the main data acquisition and processing steps carried out.

2.1. Far to Mid-Field Continuous GNSS Data

Several regional continuous GNSS networks operate stations in the mid to far-field of the epicentral area (over 10–100 km), mainly for civilian purposes. We use daily rinex data shared by the providers listed in Table S1 in Supporting Information S1 for 15 stations in total, ranging from 19 December 2020 to 20 January 2021, that is, 10 days before and 21 days after the main shock (29 December 2020, at 11:19:54 UTC). We conduct both static daily and kinematic processing to properly estimate coseismic offsets. Both techniques provide very similar coseismic offset estimates, arguing for the absence of significant pre- or post-seismic motion. We assume the coseismic offsets corresponding to the differences between the average positions before and after the earthquake in the daily time-series as the best constrained (Figure 1 and Data Set S1 in Supporting Information S1), and use these offsets in modeling (see Section 3.2).

2.2. Benchmark Measurements

Soon after the earthquake, 169 geodetic benchmarks were measured on the field (from 8 January to 5 May 2021, Kordić et al. (2021)). These benchmarks (fixed in the asphalt with uncertain coupling to bedrock) are part of cadastral or topographic networks that are usually surveyed with techniques providing centimetric accuracy on position measurements (fast-static measurements, Figure 2c). Their post-earthquake position is obtained using a Trimble R8-3 integrated antenna-receiver system, and a bipod apparatus (Figure 2c) in place for several minutes which allows Real Time Kinematics (RTK) positioning with the Croatian Positioning Virtual Reference Station System service (VPPS service at https://www.cropos.hr/). The resulting raw positions were not postprocessed (Data Set S3 in Supporting Information S1). The accuracy of the VPPS service is 2 and 4 cm in the horizontal

19448007, 2022, 24, Downloaded from https://agupubs.onlinelibrary.wiley.com/doi/10.1029/2022GL100166 by Cochrane France, Wiley Online Library on [17/12/2022]. See the Terms and Conditions (https://onlinelibrary.wiley.com/terms-and-conditions) on Wiley Online Library for rules of use; OA articles are governed by the applicable Creative Commons License

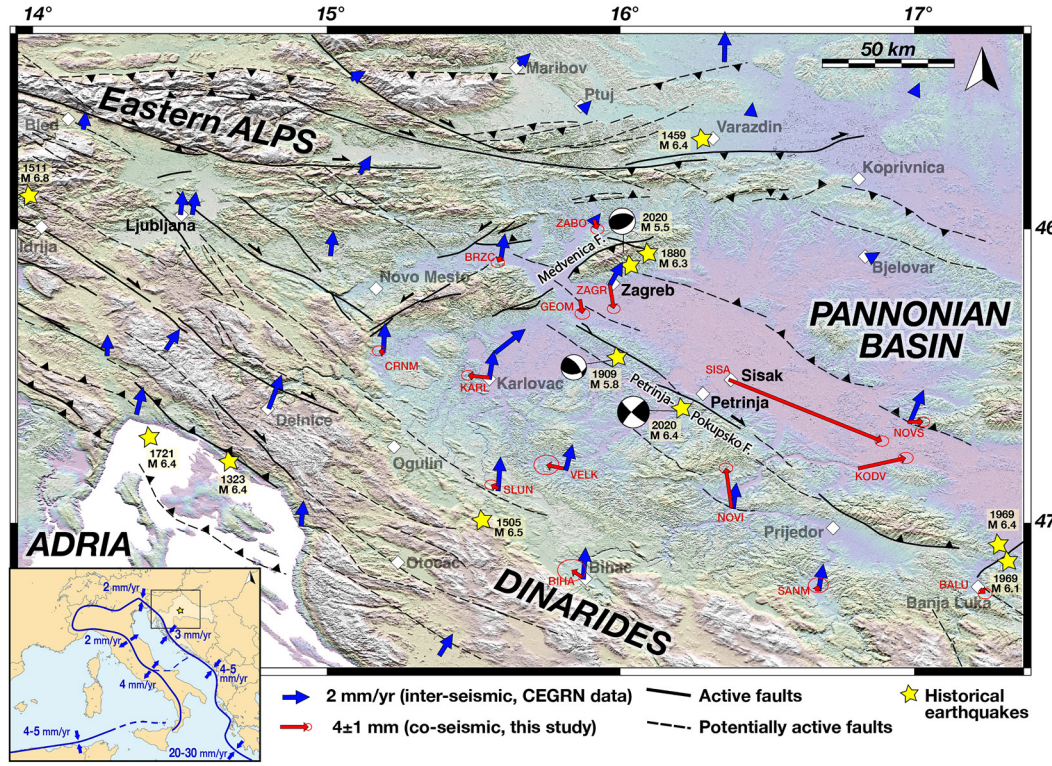

Figure 1. Coseismic displacements (red arrows) calculated at continuous GNSS stations by taking the difference between the averaged position before and after the earthquake based on daily time-series (Data Set S1 in Supporting Information S1). Interseismic velocities (blue arrows) are plotted relative to stable Eurasia (Zurutuza et al., 2019). Focal mechanisms of historical earthquakes are plotted together with known active or potentially active faults (see Baize et al. (2022) and references therein). Inset: present-day regional kinematics (Nocquet, 2012).

and vertical direction, respectively (Kordić et al., 2021; Pavasović et al., 2016), but these values are probably underestimated. Indeed, the network of base stations used by the CROatian POsitioning System (CROPOS) service was modified after the main shock and the corrections coming from the nearest continuous station (SISA) were discarded until mid-february due to its large coseismic motion. The measurements were therefore obtained with corrections coming from the remaining distant (>50 km) bases. Since the accuracy of RTK measurements decreases with distance to base stations (1 cm/10 km distance), one would expect larger uncertainties for measurements made before 15 January 2021.

Several issues need to be tackled in order to derive reliable coseismic offsets. First, post-earthquake positions may be affected by the coseismic motion that deformed the VPPS base stations network and that was not fully corrected. As the coseismic motion of distant base stations is relatively small (<1 cm, Figure 2), we neglect this effect. Second, part of the measured displacement is biased by interseismic loading and post-seismic motion. Although the pre-seismic displacement rates are poorly constrained in the area (Metois et al., 2015), we apply the Bayesian inversion method developed by Pagani et al. (2021) to interpolate the available horizontal interseismic velocity fields (Metois et al., 2015; Zurutuza et al., 2019). We find interseismic velocities of 2.3 ± 0.3 mm/yr to the East and 0.5 ± 0.1 mm/yr to the North, resulting in corrections lower than 1 cm for our data set. A maximum of 3 cm of post-seismic East-West motion is expected based on published InSAR data (Baize et al., 2022), north of the rupture tip where our benchmark network is sparse (Figure 2). Since the benchmarks are measured over different time spans, there is no simple way to properly correct from this postseismic signal and we have chosen not to apply any correction. Finally, the coseismic displacement field seems unaffected by landslides or liquefaction zones (from Baize et al. (2022)), except for one station near Sisak that was therefore discarded (Figure 2 and Data Set S2 in Supporting Information S1).

19448007, 2022, 24, Downloaded from https://agupubs.onlinelibrary.wiley.com/doi/10.1029/2022GL100166 by Cochrane France, Wiley Online Library on [17/12/2022]. See the Terms and Conditions (https://onlinelibrary.wiley.com/terms-and-conditions) on Wiley Online Library for rules of use; OA articles are governed by the applicable Creative Commons License

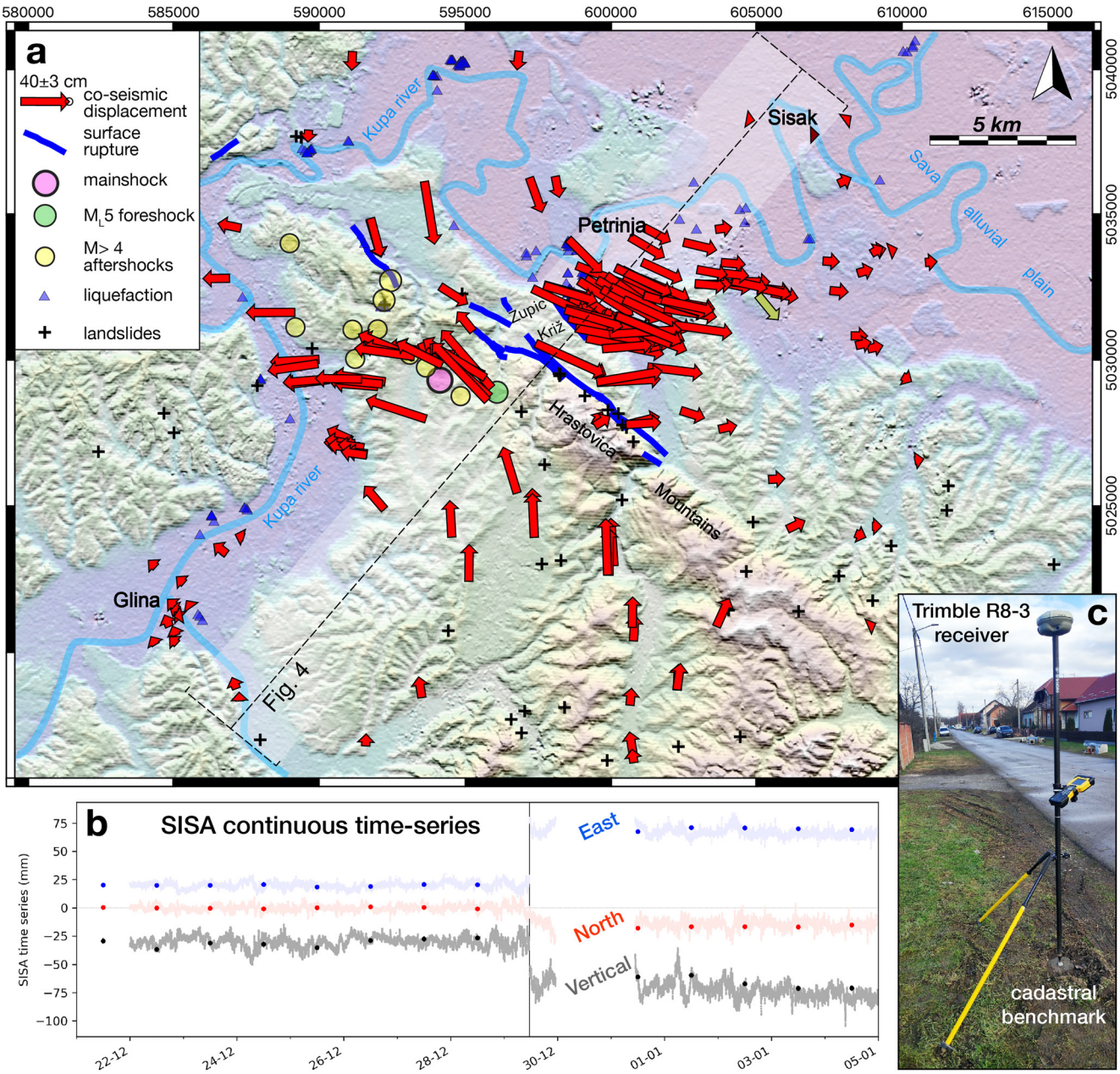

Figure 2. (a) Red arrows: coseismic horizontal displacements measured at civilian benchmarks and corrected from theoretical pre-earthquake interseismic motion. Uncertainties are not plotted for clarity. Green arrow: displacement excluded due to local inconsistency. Seismic catalog, surface rupture evidences, traces of liquefaction or coseismic landslides are extracted from Baize et al. (2022). (b) Daily time-series of continuous station SISA (Sisak city). The station was shut down for more than 1 day after the earthquake. (d) A typical set up for civilian benchmark measurements.

2.3. Coseismic Deformation Pattern

Figure 1 shows that the coseismic offsets calculated in the mid to far-field from the epicentral area are consistent with the observed right-lateral mechanism of the main shock (see also a comparison between the presented GNSS measurements and the available InSAR data in the Figure S1 in Supporting Information S1). No significant surface displacement is measured at distances greater than 90 km. Over the short time span covered by the continuous GNSS time-series (i.e., in the 20 days following the earthquake), no clear post-seismic signal is observed, consistently with preliminary post-seismic InSAR maps (Baize et al., 2022; Ganas et al., 2021). The extension of the post-seismic signal that has been observed in the very near-field of the fault is likely limited to localized afterslip (Baize et al., 2022; Ganas et al., 2021). The horizontal coseismic displacements measured

19448007, 2022, 24, Downloaded from https://agupubs.onlinelibrary.wiley.com/doi/10.1029/2022GL100166 by Cochrane France, Wiley Online Library on [17/12/2022]. See the Terms and Conditions (https://onlinelibrary.wiley.com/terms-and-conditions) on Wiley Online Library for rules of use; OA articles are governed by the applicable Creative Commons License

19448007, 2022, 24, Downloaded from https://agupubs.onlinelibrary.wiley.com/doi/10.1029/2022GL100166 by Cochrane France, Wiley Online Library on [17/12/2022]. See the Terms and Conditions (https://onlinelibrary.wiley.com/terms-and-conditions) on Wiley Online Library for rules of use; OA articles are governed by the applicable Creative Commons License

on benchmarks (Figures 2 and 4) are remarkably consistent with the expected pattern. To the east of the fault trace, the Petrinja basin moves south and rotates counterclockwise. The westernmost area moves northeast with a counterclockwise motion. The maximum horizontal displacement obtained near the epicenter is ~69 cm. One can notice that the horizontal motion is close to but not zero in the Glina valley located more than 15 km southeastward of the fault trace.

Figure 3 shows the fault-perpendicular and fault-parallel components of the horizontal displacements across the fault. While the fault-perpendicular component is rather scattered in particular west of the fault trace, the fault-parallel displacement profile exhibits to the first order a clear arc-tangent shape centered on the main fault (F1) (Figure 3c). Such pattern predicted by the elastic rebound theory is typical of strike-slip earthquakes on a single subvertical fault. In more detail, however, the maximum fault-parallel motion is observed 2.5 km east of the main fault trace, associated with a secondary amplitude peak along the profile (Figure 3d).

3. Coseismic Slip Inversion

3.1. Model Parameterization and Inversion Method

We use the Tdefnode program (McCaffrey, 2009) to invert for the coseismic slip distribution on a single fault plane that best fits our displacement field. The code solves the equations from (Okada, 1985) relating surface displacements to slip on dislocations at depth within a homogeneous elastic half-space. We use the mapped surface rupture and the published hypocenters distribution (Baize et al., 2022) to constrain the geometry and position of the fault which is 28 km-long with a strike of N130°, and extends up to 14 km at depth. The fault is discretized into 2 km wide sub-faults defined by 15 independent nodes along-strike and 8 along-dip. We perform inversions with different dips of the fault ranging from purely vertical to 70°SW, in agreement with the available data (Baize et al., 2022; Xiong et al., 2022). We invert for the rake and slip amplitude at each node using the horizontal components of both continuous GNSS and civilian benchmark displacements. The vertical component from these data sets is discarded, however, we ensure that the solutions are within the large uncertainties and wide distribution of these measurements (Figure S2 in Supporting Information S1). We constrain the scalar seismic moment (Aki, 1967) to be between 1×10^{18} and 6×10^{18} Nm, and set uncertainties to 3 cm for benchmark displacements (a minimum estimate).

Simulated annealing and grid search techniques are used to converge toward an optimal model that minimizes the sum of the reduced chi-square statistic. We use a Laplacian smoothing on the slip distribution to avoid numerical instabilities (McCaffrey, 2009). The degree of smoothing is chosen following the L-curve approach, finding a compromise between the average slip gradient (or solution roughness in cm/km, Jónsson et al. (2002)) and the misfit function (defined by McCaffrey (2009) as the reduced Chi^2) for each obtained alternative model (Figures S3 and S4 in Supporting Information S1).

3.2. Model Resolution

To evaluate the ability of GNSS observations to constrain slip at depth, we calculate the sensitivity of the data set to unit displacements on each subfault, following the method of Loveless and Meade (2011) (Figure S5 in Supporting Information S1). Overall, the sensitivity is relatively high from the surface down to 5 km depth in the central part of the rupture where most of the ground ruptures are observed (Baize et al., 2022). The sensitivity largely decreases at the fault edges and under 10 km depth. Complementary checkerboard tests are conducted with varying checkerboard size (Figure S6 in Supporting Information S1). They confirm that our data set is able to constrain shallow slip patterns (<7 km). The position and size of slip asperities larger than 3 km are well retrieved along strike, while their slip amplitude may be slightly overestimated.

3.3. Results

We tested different smoothing factors and obtained trade-off curves between solution roughness and misfit for each fault-dip in the 70–90°SW-dipping range (Figures S3 and S4 in Supporting Information S1). Our preferred solution (black lines in Figures 3 and 4) is obtained for a vertical fault (90°) and a moderate smoothing (roughness = 0.025 cm/km), but alternative models with an overall misfit lower than 18 (see Figure S4 in Supporting Information S1) also shows acceptable fit to the data with fault dip between 82 and 90°SW and slip roughness

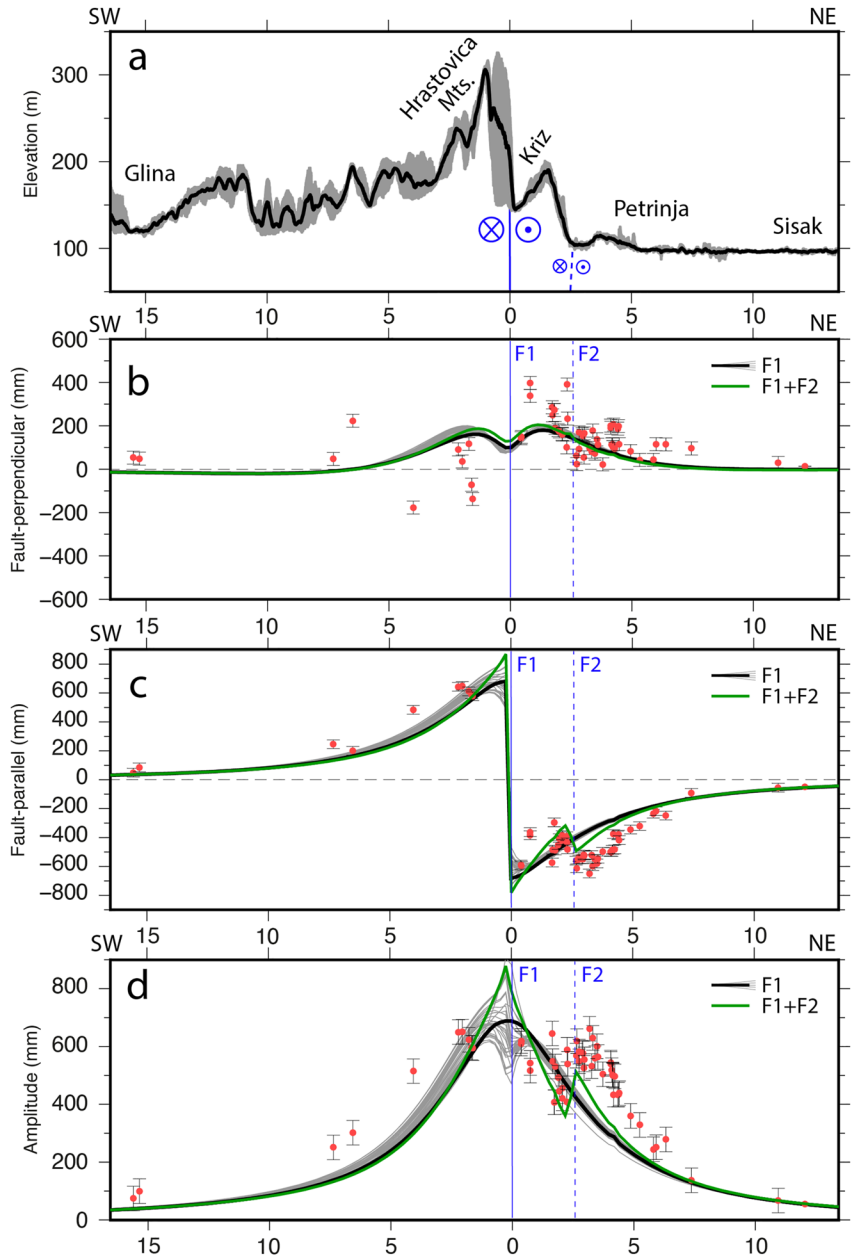

Figure 3. Topography ((a), from https://www.eorc.jaxa.jp/ALOS/en/dataset/aw3d30/aw3d30_e.htm) and horizontal coseismic displacements along the SW-NE profile line shown in Figure 2: (b) fault-perpendicular component, (c) fault-parallel component, and (d) norm of the amplitude, for measured displacements (red dots) with associated uncertainties and modeled ones (black lines). Gray curves are predicted displacements for a set of alternative models (misfit <18, slip roughness >0.02 cm/km, fault dip between 82 and 90°SW). Green curve is the 2-fault solution. See discussion in text and Supporting Information S1 for details. The position of the main fault (F1) and secondary fault (F2) used in the modeling is represented in blue. Note that they correspond to topographic steps SW of Križ and Petrinja.

>0.02 cm/km (gray lines, Figures 3 and 4). The associated scalar moment is 3.9×10^{18} Nm, with a slip peak reaching 3.7 m. Interestingly, their associated seismic moments ($3.88 \pm 0.02 \times 10^{18}$ Nm) and slip peak value (4.9 ± 0.7 m) are very similar, and therefore well constrained.

The best solutions all exhibit patches of localized slip at depths less than 7 km that extend over 18 km along-strike (Figures 4b and 4c). Our preferred solution requires significant surface slip since a right-lateral displacement of 50 cm on average is needed over a ~10 km long portion of the fault to fit the data (Figures 4a and 4b).

19448007, 2022, 24, Downloaded from https://agupubs.onlinelibrary.wiley.com/doi/10.1029/2022GL100166 by Cochrane France, Wiley Online Library on [17/12/2022]. See the Terms and Conditions (https://onlinelibrary.wiley.com/terms-and-conditions) on Wiley Online Library for rules of use; OA articles are governed by the applicable Creative Commons License

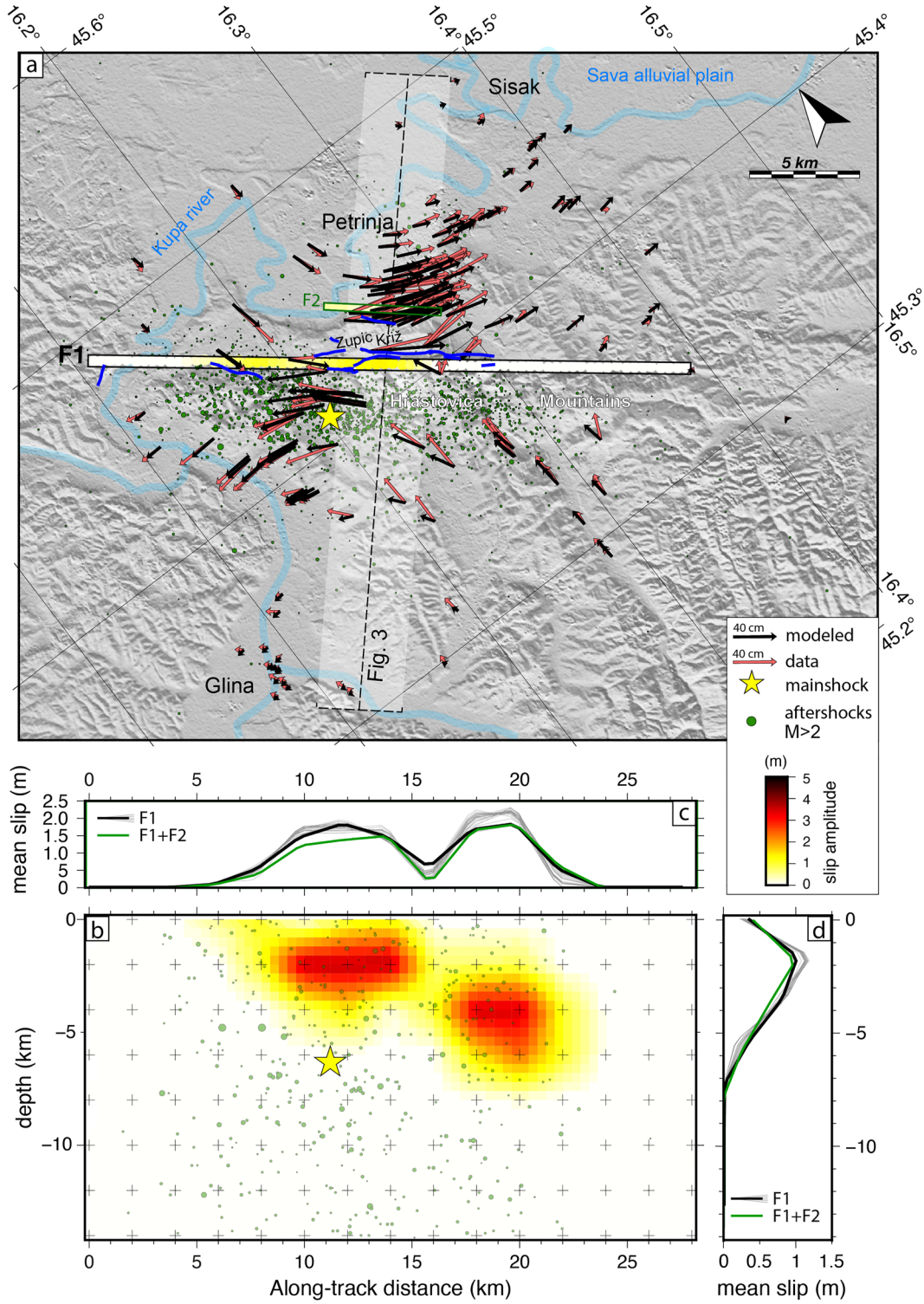

Figure 4. (a) Observed (black vectors) and predicted (red vectors) coseismic displacements from our preferred model. Surface slip along the main fault (F1) is color coded. Blue lines: observed surface rupture (Baize et al., 2022). F2 stands for a sub-parallel secondary fault that may have slipped during earthquake. (b) Coseismic slip distribution on F1 plane for our preferred model. (c) Along-strike and (d) along-dip variations of the averaged coseismic slip are presented for the preferred solution (black) and a set of alternative models (gray). Green curves: same but for the 2-fault model including coseismic slip on F2. Green circles and yellow star: aftershocks and main shock from Baize et al. (2022). Most aftershocks occurred between 3 and 23 km along strike.

19448007, 2022, 24, Downloaded from https://agupubs.onlinelibrary.wiley.com/doi/10.1029/2022GL100166 by Cochrane France, Wiley Online Library on [17/12/2022]. See the Terms and Conditions (https://onlinelibrary.wiley.com/terms-and-conditions) on Wiley Online Library for rules of use; OA articles are governed by the applicable Creative Commons License

19448007, 2022, 24, Downloaded from https://agupubs.onlinelibrary.wiley.com/doi/10.1029/2022GL100166 by Cochrane France, Wiley Online Library on [17/12/2022]. See the Terms and Conditions (https://onlinelibrary.wiley.com/terms-and-conditions) on Wiley Online Library for rules of use; OA articles are governed by the applicable Creative Commons License

The maximum surface displacement (1 m) is reached near Križ. Note that the inverted slip pattern at depth is composed of two patches (Figure 4) whatever the roughness or the dip of the model considered. The main patch is 10 km-long, has a slip peak of 3.67 m, and extends from surface to 4 km depth. A ∼7 km wide and deeper patch (2–7 km deep) lies to the southeast, with a slip peak reaching 3.5 m (Figure 4). The lower coseismic slip region between the two patches is consistent over the range of selected models (see Figure 4b).

Our preferred model fits the different data sets well, with nRMS values of 5.1 for the continuous GNSS (associated with low and probably underestimated uncertainties) and 1.4–5.8 for the benchmark data sets (Figures S7 and S8 in Supporting Information S1). Residual displacements are observed in the near-field (6.4 cm in average), with systematic residues near Petrinja and Glina (Figure S7 in Supporting Information S1). This is also apparent in Figure 3: our best models fail in recovering the exact shape of the fault-parallel displacements and displacement amplitude in the Petrinja area, 2.5 km east from the main fault trace, and underestimate the velocities observed in the western compartment.

4. Discussion and Conclusion

The dip (82–90°), strike (130°), and rake (184.6° ± 1.6°) from our preferred and alternative models (Figure 4 and Figure S4 in Supporting Information S1) are close to published focal mechanism solutions (70–89, 128–134, and 167°–180°, respectively, Baize et al. (2022)) and consistent with the long-term morphology of the PPKF and surface ruptures mapped on the field (Baize et al., 2022). Our preferred coseismic slip model (Figure 4) also share common characteristics with InSAR-based solutions outlining at shallow depths (<7 km) a highly steeping (76–84°SW) planar rupture, <6 km wide, with peak slip values reaching 3.5 m (Ganas et al., 2021; Xiong et al., 2022). Indeed, the GNSS-based models confirm a shallow rupture (<7 km) with strike-slip amounts of 4.88 ± 0.69 m (∼3.7 m for the preferred smoothed solution) and high dipping angles (82–90°SW). We note that our final slip estimate may be slightly overestimated as our data set contains postseismic motion that has not been corrected. However, the lack of clear correlation between the model nRMS and the post-seismic date of acquisition suggests a minor contribution of the afterslip phase compared to the co-seismic one (Figures S8 in Supporting Information S1).

Preliminary InSAR-based models first suggested that the rupture did not reach the surface (Ganas et al., 2021), while our models as the one from Xiong et al. (2022) support surface slip on the order of ∼1 m over 9 km along-strike, in agreement with the ∼13 km long surface rupture derived from field observations (Baize et al., 2022). However, our models differ from the single slip patch (Xiong et al., 2022) or homogenous slip solution (Ganas et al., 2021) suggested by InSAR-based studies. Indeed, two slip patches are inferred from our inversions, with a total length of ∼17 km at 2–3 km depth. The variations of the average slip along strike and dip (Figure 4) appear robust, as they are stable over the range of tested parameters. Our sensitivity tests also show that both patches are well resolved, allowing for further interpretations. This complexity could result from diverging constraints in the near-field as the GNSS data coverage is denser and more reliable than InSAR data, which show clear decorrelation along-strike (Ganas et al. (2021); Xiong et al. (2022), and Figure S1 in Supporting Information S1).

Even if the fit of our first-order 1-fault model to the data is good, the remaining systematic residuals in the Petrinja area (see Section 2.3) prompted us to refine our model parameterization. The deviation of observations from our best-model occurs 2.5 km north of the main fault trace (Figure 3), at the Križ topographic front, where secondary surface ruptures have been mapped (see Figures 2 and 4). We therefore explore a 2-fault inversion in which the observed displacements result from coseismic slip both on the PPKF and on a secondary, parallel fault (F2, see Figures 3 and 4) at the foot of this topographic front, striking 130°N and dipping 90°. The amount of homogeneous slip is inverted on F2 together with the rake and fault dimension. Model setting for the PPKF is similar to our 1-fault model. We find that an additional 5.4 km long × 10 km wide dislocation centered at 5 km depth, with a uniform total slip of 0.29 m, improves the fit to the data (mean nRMS is reduced from 3.38 to 3.12), in particular in the Petrinja area (see Figure 3 and Figure S9 in Supporting Information S1). In this 2-fault model, slip on the PPKF and on the secondary fault F2 accounts for equivalent M_w 6.29 and 5.7 events, respectively. The resulting slip distribution on the PPKF is very similar to our preferred 1-fault solution (Figure S9 in Supporting Information S1 and green curves in Figures 3 and 4).

19448007, 2022, 24, Downloaded from https://agupubs.onlinelibrary.wiley.com/doi/10.1029/2022GL100166 by Cochrane France, Wiley Online Library on [17/12/2022]. See the Terms and Conditions (https://onlinelibrary.wiley.com/terms-and-conditions) on Wiley Online Library for rules of use; OA articles are governed by the applicable Creative Commons License

Both our 1-fault and 2-faults models suggest that a significant amount of slip has reached the surface in the Župić area, which coincide with most of the surface rupture observations (Figure 2). Slip deepens to the southeast under the Hrastovica mountains. The transition from shallow to deep slip occurs between the two slip patches, suggesting an along-strike segmentation of the PPKF. Such segmentation is consistent with the complex 2020 surface rupture observed in the field (Baize et al., 2022), although the main fault stepover at the surface appears to be located between Župić and Križ, that is, 2.5 km north of the transition zone retrieved in our slip solutions (Figure 2). Our 2-faults model is consistent with the activation of a branch of the flower-like structure of the PPKF transpressive system as imaged by seismic reflection (Baize et al., 2022). Such synchronous ruptures on neighboring faults within the same fault-system is commonly described during $M_w > 6$ strike-slip events (Antoine et al., 2021; Toda et al., 2016; Wang et al., 2018; Xu et al., 2009). They could sign a low fault structural maturity (Perrin et al., 2016), consistent with the multi-strand morphotectonic signature of the PPKF (Baize et al., 2022). These complex ruptures could also correspond to slip partitioning between strike-slip and thrust (Daout et al., 2016; Toda et al., 2016), which would be consistent with the flower structure and transpressional setting of the PPKF. However, the dip-slip motion from our data set and inversion models is minor compared to the strike-slip component (<20% on F1 and <25% on F2). A more detailed analysis, combining InSAR and optical correlation data and a varying secondary fault geometry, will help to better assess its potential reverse component. Nevertheless, this analysis do not support the hypothesis of a NE-SW oriented left-lateral conjugate fault as proposed by Markušić et al. (2021) and Tondi et al. (2021).

The new and unusual data set presented in this study provides a 3D displacement field that is consistent with the expected coseismic pattern, even though it is associated with large uncertainties. We are therefore confident that rapid remeasurements of civilian networks in case of earthquakes in poorly instrumented areas could be successfully employed if the surface deformation is higher than the centimeter level. It could change the game by improving considerably our knowledge about moderate-size earthquakes. The rapid-positioning techniques like standard RTK or VRS-RTK are getting more and more usual (Shafri & Sulaiman, 2009), low-cost (Takasu & Yasuda, 2009), free and open-source (Ancelin et al., 2022), and accurate (Teunissen & Khodabandeh, 2015; Vollath et al., 2002). These methods are starting to get used in the Earth Sciences community (Ohta et al., 2012), opening new perspectives for rapid monitoring during crisis. After an earthquake, very dense and systematic measurements could be conducted simultaneously over pre-existing civilian networks in the epicentral area in the days following the main shock. But it requires sufficient manpower and available RTK rovers, unaffected RTK/VRS networks of base stations during the earthquake and existing regional digital database of geodetic benchmarks. To ensure final uncertainties as low as possible, these networks of civilian benchmarks could be regularly measured outside of crisis periods to get well constrained pre-earthquake positions.

Data Availability Statement

All data sets and materials underlying this study are published open access in the zenodo repository https://doi.org/10.5281/zenodo.7229324, and additional details are provided in Supporting Information S1. Topographic data are from the Japan Aerospace Exploration Agency (https://www.eorc.jaxa.jp/ALOS/en/dataset/aw3d30/aw3d30_e.htm).

Acknowledgments

The coseismic offset data base used in this study is available as Supporting Information S1. The InSAR data shown in the Supporting Information S1 are from LiCSAR which contains modified Copernicus Sentinel data (2020–2021) analyzed by the Centre for the Observation and Modelling of Earthquakes, Volcanoes and Tectonics (COMET). LiCSAR uses JASMIN, the UK's collaborative data analysis environment (http://jasmin.ac.uk). Special thanks are due to O. Šukalić (State Geodetic Administration), M. Lukic (Geomediator), I. Hodalj (GeoHodalj), I. Jurić (GeoNivo), T. Stojanović (GeoBiro), L. Šlabek (Geoperfect), I. Skenderović (UOIG Skenderović), M. Grebner (Geosoft), D. Bačelić (GEOIS), D. Uljarević (MSAN nekretnine), and A. Gavran (MIG) for sharing database of civilian benchmarks. We are grateful to N. Smolčak (Geomatika-Smolcak), S. Tucikešić (Faculty of Architecture, Civil Engineering and Geodesy, University of Banja Luka), N. Fabiani (SIGNAL network), M. Marjanović and M. Ciprijan (CROPOS network), H. Kaljun and E. Redžepagić (FBiHPOS network) for providing access to permanent GNSS stations data, as well as J. Barbača, R. Filjak, D. Palenik, M. Budić (Croatian Geological Survey) for field survey assistance. This work has been conducted in the frame of a consortium of researchers that have received fundings from the programme TelluS of the Institut National des Sciences de l'Univers, CNRS, and from the CNES in the frame of the Balkasar project, focused on Sentinel-1. M. Henriquet benefits from a CNES postdoctoral fellowship. The authors would like to thank J. Ancelin for useful discussion.

References

Aki, K. (1967). Scaling law of seismic spectrum. *Journal of Geophysical Research*, *72*(4), 1217–1231. https://doi.org/10.1029/jz072i004p01217

Ancelin, J., Heintz, W., Moura, J., & Péneau, S. (2022). jancelin/docs-centipedertk: V2.2 [Dataset]. Zenodo. https://doi.org/10.5281/zenodo.5814773

Antoine, S. L., Klinger, Y., Delorme, A., Wang, K., Bürgmann, R., & Gold, R. D. (2021). Diffuse deformation and surface faulting distribution from submetric image correlation along the 2019 Ridgecrest, California, ruptures. *Bulletin of the Seismological Society of America*, *111*(5), 2275–2302. https://doi.org/10.1785/0120210036

Baize, S., Amoroso, S., Belić, N., Benedetti, L., Boncio, P., Budić, M., et al. (2022). Environmental effects and seismogenic source characterization of the December 2020 earthquake sequence near Petrinja, Croatia. *Geophysical Journal International*, *230*(2), 1394–1418. https://doi.org/10.1093/gji/ggac123

Chiaraluce, L., Di Stefano, R., Tinti, E., Scognamiglio, L., Michele, M., Casarotti, E., et al. (2017). The 2016 central Italy seismic sequence: A first look at the mainshocks, aftershocks, and source models. *Seismological Research Letters*, *88*(3), 757–771. https://doi.org/10.1785/0220160221

Daout, S., Jolivet, R., Lasserre, C., Doin, M.-P., Barbot, S., Tapponnier, P., et al. (2016). Along-strike variations of the partitioning of convergence across the Haiyuan fault system detected by InSAR. *Geophysical Supplements to the Monthly Notices of the Royal Astronomical Society*, *205*(1), 536–547. https://doi.org/10.1093/gji/ggw028

Ganas, A., Elias, P., Briole, P., Cannavo, F., Valkaniotis, S., Tsironi, V., & Partheniou, E. I. (2020). Ground deformation and seismic fault model of the M6. 4 Durres (Albania) Nov. 26, 2019 earthquake, based on GNSS/InSAR observations. *Geosciences*, *10*(6), 210. https://doi.org/10.3390/geosciences10060210

Ganas, A., Elias, P., Valkaniotis, S., Tsironi, V., Karasante, I., & Briole, P. (2021). *Petrinja earthquake moved crust 10 feet*. Temblor.

Hastaoglu, K., & Sanli, D. (2011). Accuracy of GPS rapid static positioning: Application to Koyulhisar landslide, central Turkey. *Survey Review*, *43*(321), 226–240. https://doi.org/10.1179/003962611x12894696205145

Herak, D., & Herak, M. (2010). The Kupa Valley (Croatia) earthquake of 8 October 1909—100 years later. *Seismological Research Letters*, *81*(1), 30–36. https://doi.org/10.1785/gssrl.81.1.30

Herak, D., Herak, M., & Tomljenović, B. (2009). Seismicity and earthquake focal mechanisms in North-Western Croatia. *Tectonophysics*, *465*(1–4), 212–220. https://doi.org/10.1016/j.tecto.2008.12.005

Jónsson, S., Zebker, H., Segall, P., & Amelung, F. (2002). Fault slip distribution of the 1999 M_w 7.1 hector mine, California, earthquake, estimated from satellite radar and GPS measurements. *Bulletin of the Seismological Society of America*, *92*(4), 1377–1389. https://doi.org/10.1785/0120000922

Kordić, B., Vukovski, M., Budić, M., Špelić, M., Barbača, J., Belić, N., et al. (2021). Geodetic benchmark displacement measurements following the 2020 Petrinja earthquake in Croatia. In *EGU General Assembly Conference Abstracts*, (p. EGU21–16588).

Loveless, J. P., & Meade, B. J. (2011). Spatial correlation of interseismic coupling and coseismic rupture extent of the 2011 $M_w = 9.0$ Tohoku-oki earthquake. *Geophysical Research Letters*, *38*(17), L17306. https://doi.org/10.1029/2011gl048561

Markušić, S., Stanko, D., Korbar, T., Belić, N., Penava, D., & Kordić, B. (2020). The Zagreb (Croatia) M5.5 earthquake on 22 March 2020. *Geosciences*, *10*(7), 252. https://doi.org/10.3390/geosciences10070252

Markušić, S., Stanko, D., Penava, D., Ivančić, I., Bjelotomić Oršulić, O., Korbar, T., & Sarhosis, V. (2021). Destructive M6.2 Petrinja earthquake (Croatia) in 2020—Preliminary multidisciplinary research. *Remote Sensing*, *13*(6), 1095. https://doi.org/10.3390/rs13061095

McCaffrey, R. (2009). Time-dependent inversion of three-component continuous GPS for steady and transient sources in northern Cascadia. *Geophysical Research Letters*, *36*(7), L07304. https://doi.org/10.1029/2008gl036784

Metois, M., D'Agostino, N., Avallone, A., Chamot-Rooke, N., Rabaute, A., Duni, L., et al. (2015). Insights on continental collisional processes from GPS data: Dynamics of the peri-Adriatic belts. *Journal of Geophysical Research: Solid Earth*, *120*(12), 8701–8719. https://doi.org/10.1002/2015jb012023

Nocquet, J.-M. (2012). Present-day kinematics of the Mediterranean: A comprehensive overview of GPS results. *Tectonophysics*, *579*, 220–242. https://doi.org/10.1016/j.tecto.2012.03.037

Ohta, Y., Kobayashi, T., Tsushima, H., Miura, S., Hino, R., Takasu, T., et al. (2012). Quasi real-time fault model estimation for near-field tsunami forecasting based on RTK-GPS analysis: Application to the 2011 Tohoku-Oki earthquake (M_w 9.0). *Journal of Geophysical Research*, *117*(B2), B02311. https://doi.org/10.1029/2011jb008750

Okada, Y. (1985). Surface deformation due to shear and tensile faults in a half-space. *Bulletin of the Seismological Society of America*, *75*(4), 1135–1154. https://doi.org/10.1785/bssa0750041135

Pagani, C., Bodin, T., Métois, M., & Lasserre, C. (2021). Bayesian estimation of surface strain rates from global navigation satellite system measurements: Application to the southwestern United States. *Journal of Geophysical Research: Solid Earth*, *126*(6), e2021JB021905. https://doi.org/10.1029/2021JB021905

Pavasović, M., Marjanović, M., Bašić, T., & Vjesnik, T. (2016). Towards the new Croatian terrestrial reference frame based on CROPOS—Preliminary results. *Technical Gazette*, *23*(3), 893–897. https://doi.org/10.17559/TV-20141114153027

Perrin, C., Manighetti, I., Ampuero, J.-P., Cappa, F., & Gaudemer, Y. (2016). Location of largest earthquake slip and fast rupture controlled by along-strike change in fault structural maturity due to fault growth. *Journal of Geophysical Research: Solid Earth*, *121*(5), 3666–3685. https://doi.org/10.1002/2015jb012671

Pesci, A., Loddo, F., Teza, G., Cenni, N., & Casula, G. (2008). Analyzing virtual reference station for GPS surveying: Experiments and applications in a test site of the northern Apennine (Italy). *Annals of Geophysics*, *51*(4).

Prelogović, E., Saftić, B., Kuk, V., Velić, J., Dragaš, M., & Lučić, D. (1998). Tectonic activity in the Croatian part of the Pannonian basin. *Tectonophysics*, *297*(1–4), 283–293. https://doi.org/10.1016/s0040-1951(98)00173-5

Shafri, H., & Sulaiman, S. (2009). GPS survey accuracy using virtual reference station (VRS) outside the Malaysian real-time kinematic network (MyRTKnet) services. *International Journal of Geoinformatics*, *5*(2), 39–45.

Takasu, T., & Yasuda, A. (2009). Development of the low-cost RTK-GPS receiver with an open source program package RTKLIB. In *International symposium on GPS/GNSS* (Vol. 1). International Convention Center Jeju Korea.

Teunissen, P., & Khodabandeh, A. (2015). Review and principles of PPP-RTK methods. *Journal of Geodesy*, *89*(3), 217–240. https://doi.org/10.1007/s00190-014-0771-3

Toda, S., Kaneda, H., Okada, S., Ishimura, D., & Mildon, Z. K. (2016). Slip-partitioned surface ruptures for the M_w 7.0 16 April 2016 Kumamoto, Japan, earthquake. *Earth Planets and Space*, *68*(1), 1–11. https://doi.org/10.1186/s40623-016-0560-8

Tomljenović, B., & Csontos, L. (2001). Neogene–quaternary structures in the border zone between alps, Dinarides and Pannonian Basin (Hrvatsko zagorje and Karlovac basins, Croatia). *International Journal of Earth Sciences*, *90*(3), 560–578. https://doi.org/10.1007/s005310000176

Tondi, E., Blumetti, A. M., Čičak, M., Di Manna, P., Galli, P., Invernizzi, C., et al. (2021). "Conjugate" coseismic surface faulting related with the 29 December 2020, M_w 6.4, Petrinja earthquake (Sisak-Moslavina, Croatia). *Scientific Reports*, *11*(1), 1–15. https://doi.org/10.1038/s41598-021-88378-2

Vollath, U., Landau, H., & Chen, X. (2002). Network RTK–concept and performance. In *Proceedings of the GNSS symposium* (pp. 27–30).

Wang, T., Wei, S., Shi, X., Qiu, Q., Li, L., Peng, D., et al. (2018). The 2016 Kaikōura earthquake: Simultaneous rupture of the subduction interface and overlying faults. *Earth and Planetary Science Letters*, *482*, 44–51. https://doi.org/10.1016/j.epsl.2017.10.056

Xiong, W., Yu, P., Chen, W., Liu, G., Zhao, B., Nie, Z., & Qiao, X. (2022). The 2020 M_w 6.4 Petrinja earthquake: A dextral event with large coseismic slip highlights a complex fault system in northwestern Croatia. *Geophysical Journal International*, *228*(3), 1935–1945. https://doi.org/10.1093/gji/ggab440

Xu, X., Wen, X., Yu, G., Chen, G., Klinger, Y., Hubbard, J., & Shaw, J. (2009). Coseismic reverse-and oblique-slip surface faulting generated by the 2008 M_w 7.9 Wenchuan earthquake, China. *Geology*, *37*(6), 515–518. https://doi.org/10.1130/g25462a.1

Zurutuza, J., Caporali, A., Bertocco, M., Ishchenko, M., Khoda, O., Steffen, H., et al. (2019). The central European GNSS research network (CEGRN) dataset. *Data in Brief*, *27*, 104762. https://doi.org/10.1016/j.dib.2019.104762

19448007, 2022, 24, Downloaded from https://agupubs.onlinelibrary.wiley.com/doi/10.1029/2022GL100166 by Cochrane France, Wiley Online Library on [17/12/2022]. See the Terms and Conditions (https://onlinelibrary.wiley.com/terms-and-conditions) on Wiley Online Library for rules of use; OA articles are governed by the applicable Creative Commons License

References From the Supporting Information

Bar-Sever, Y. E., Kroger, P. M., & Borjesson, J. A. (1998). Estimating horizontal gradients of tropospheric path delay with a single GPS receiver. *Journal of Geophysical Research*, *103*(B3), 5019–5035. https://doi.org/10.1029/97jb03534

Bertiger, W., Bar-Sever, Y., Dorsey, A., Haines, B., Harvey, N., Hemberger, D., et al. (2020). GipsyX/RTGx, a new tool set for space geodetic operations and research. *Advances in Space Research*, *66*(3), 469–489. https://doi.org/10.1016/j.asr.2020.04.015

Bertiger, W., Desai, S. D., Haines, B., Harvey, N., Moore, A. W., Owen, S., & Weiss, J. P. (2010). Single receiver phase ambiguity resolution with GPS data. *Journal of Geodesy*, *84*(5), 327–337. https://doi.org/10.1007/s00190-010-0371-9

Bohm, J., Niell, A., Tregoning, P., & Schuh, H. (2006). Global mapping function (GMF): A new empirical mapping function based on numerical weather model data. *Geophysical Research Letters*, *33*(7), L07304. https://doi.org/10.1029/2005gl025546

Scherneck, H.-G. (1991). A parametrized solid Earth tide model and ocean tide loading effects for global geodetic baseline measurements. *Geophysical Journal International*, *106*(3), 677–694. https://doi.org/10.1111/j.1365-246x.1991.tb06339.x

Twardzik, C., Vergnolle, M., Sladen, A., & Avallone, A. (2019). Unravelling the contribution of early postseismic deformation using sub-daily GNSS positioning. *Scientific Reports*, *9*(1), 1–12. https://doi.org/10.1038/s41598-019-39038-z

Zumberge, J., Heflin, M., Jefferson, D., Watkins, M., & Webb, F. (1997). Precise point positioning for the efficient and robust analysis of GPS data from large networks. *Journal of Geophysical Research*, *102*(B3), 5005–5017. https://doi.org/10.1029/96jb03860

19448007, 2022, 24, Downloaded from https://agupubs.onlinelibrary.wiley.com/doi/10.1029/2022GL100166 by Cochrane France, Wiley Online Library on [17/12/2022]. See the Terms and Conditions (https://onlinelibrary.wiley.com/terms-and-conditions) on Wiley Online Library for rules of use; OA articles are governed by the applicable Creative Commons License